Composite Structures 99 (2013) 123–130

Contents lists available at SciVerse ScienceDirect

Composite Structures

journal homepage: www.elsevier.com/locate/compstruct

Elastoplastic modeling of polymeric composites containing randomly located nanoparticles with an interface effect

B.J. Yang, Y.Y. Hwang, H.K. Lee *

Department of Civil and Environmental Engineering, Korea Advanced Institute of Science and Technology, Guseong-dong, Yuseong-gu, Daejeon 305-701, South Korea

A R T I C L E   I N F O

Article history:
Available online 20 December 2012

Keywords:
Nanoparticle-reinforced composite material
Elastoplastic behavior
Interface effect
Particle size effect
Micromechanics-based constitutive model

A B S T R A C T

An elastoplastic constitutive model is proposed to predict the overall behavior of nanoparticle-reinforced polymeric composites. The effective elastic moduli of nanocomposites, composed of a polymer matrix and randomly dispersed nanoparticles, are constructed by incorporating the Eshelby tensor considering the interface effect into a micromechanics-based ensemble volume-averaged method. Micromechanical homogenization procedures are utilized to estimate an effective yield function in accordance with the continuum plasticity theory and are employed to predict the overall elastoplastic behavior. The effects of the particle size, interface moduli and the strengthening influence of the nanoparticles are investigated via numerical simulations. Finally, comparisons between theoretical predictions and the available experimental data are made to assess the predictive capability of the proposed framework.

1. Introduction

Nanocomposites can be optimal candidates for numerous important applications as a result of their high stiffness, high durability and low density [9]. The remarkably different features of nanocomposites are caused by the dimensions of their nanofillers, which lie within the nanoscale. The nanoscale fillers offer a prominent mechanism to enhance the composite system, and many studies have reported that the use of nanoparticles and nanofibers increase the strength and durability of cementitious and polymeric composites [1,44]. When nanoparticles are uniformly dispersed in a polymer matrix, nanocomposites have a relatively large interface surface area compared to microscale materials [49]. The extended interface area leads to an increase in the interface effect and is demonstrated to give a significant effect on the overall behavior of the nanocomposites [4,44]; however, the contribution may be negligible when a particle size exceeds 1 μm [7].

Numerous analytical or semi-analytical solutions for nanoparticle-reinforced composites have been explored in an effort to predict their mechanical characteristics. With the concept of micromechanics, the elastoplastic behavior of amorphous nanocomposites was modeled as a three-phase heterogeneous material which instills a spherical shape in nanoparticles, with the interlayer surrounding the nanoparticles and matrix [38,4]. Further studies which focused on particle–particle, particle-interlayer and particle–matrix interactions were also conducted [24]. In addition, a model that considers the effects of the particle size, matrix degradation and the adhesion between the particles and the matrix was proposed by Li et al. [36]. Colombini et al. [3] extended the self-consistent scheme to account for the interface effect by including an interphase region, and a three-phase unit cell model based on a particle-interphase-matrix was formulated to investigate the influence of the particle stiffness and size. It was concluded from an assessment of the literature that smaller and harder particles result in greater mechanical properties of composite materials composed of latex and nano-sized particles.

Sun et al. [46] derived the effective stiffness of nanocomposites by employing bottom-up and top-down multi-scale methods based on micromechanics and compared the result with the result from FEM modeling. The mechanism of nano-TiN powder in polymeric composites was investigated in experiments and in FEM simulations [41]. Moreover, several studies adopted the molecular dynamics (MD) simulation to analyze nanocomposites. Hong et al. [8] simulated nano-Cu/FeS composites with the MD simulation and demonstrated that the mechanical properties of the nanocomposites depended on the sizes of the particles at the same exposure condition of the reinforcing phase. Yang et al. [52] introduced a scale-bridging method for nanoparticle-reinforced composites and verified it in comparisons by means of the MD simulations.

A micromechanical framework based on the conventional Eshelby theory [6] assumes that spherical inclusions are perfectly embedded in the matrix and the interface region has zero interface stress [47]. The assumption of the zero interface effect is acceptable for microscale inclusion, but it cannot accurately predict an inclusion smaller than 1 μm [7]. The current study aims to develop an effective elastoplastic model for nanoparticle-reinforced polymeric composites considering the effects of interface properties

* Corresponding author. Tel.: +82 42 350 3623.
E-mail address: leeh@kaist.ac.kr (H.K. Lee).

0263-8223/$ - see front matter © 2012 Elsevier Ltd. All rights reserved.
http://dx.doi.org/10.1016/j.compstruct.2012.11.043

and particle size. The present model successfully combines the interior and exterior Eshelby tensors for nano-scale inhomogeneity [4] and the micromechanics-based ensemble volume averaged method [10]. In order to consider the size effect on both elastic and plastic ranges, a separate derivation with an interface effect for the pre- and post-yield behavior is newly developed by means of ensemble volume averaged method. Within the present formulation, influences of interface properties, matrix plasticity, and nanoparticle size on the overall behavior of nanocomposites are discussed in detail. The capability of the present model for predicting the elastoplastic behavior of nanoparticle-reinforced composites is demonstrated through a number of numerical simulations and experimental comparisons.

2. The ensemble-average procedures

2.1. Recapitulation of effective elastic behavior of nanoparticle-reinforced composites

Following Ju et al. [13,18], a micromechanical framework for nanocomposites, composed of a polymer matrix and uniformly-dispersed nanoparticles, is summarized next. When the composites undergo a small amount of deformation, the total macroscopic strain $\bar{\epsilon}$ can be expressed as [13,34]

$$\bar{\epsilon} = \bar{\epsilon}_e + \bar{\epsilon}_p \tag{1}$$

where $\bar{\epsilon}_e$ and $\bar{\epsilon}_p$ denote the overall elastic and plastic strain, respectively. The effective elastic stress–strain relationship can be written as [18,32,33,29]

$$\bar{\boldsymbol{\sigma}} = \mathbf{C}_* : \bar{\epsilon}_e \tag{2}$$

where the effective elastic moduli of composites $\mathbf{C}_*$, as derived by Ju and Chen [10,11], is as follows (cf. [29,25,45,50,51]):

$$\mathbf{C}_* = \mathbf{C}_0 \cdot \left\{ \mathbf{I} + \mathbf{B} \cdot (\mathbf{I} - \mathbf{S} \cdot \mathbf{B})^{-1} \right\} \tag{3}$$

with

$$\mathbf{B} = \phi_1 \left\{ \mathbf{S} + (\mathbf{C}_1 - \mathbf{C}_0)^{-1} \cdot \mathbf{C}_0 \right\}^{-1} \tag{4}$$

where "·" denotes the tensor multiplication, and the subscripts 0 and 1 respectively denote the matrix and the nanoparticle phase; $\mathbf{C}_q$ is the elastic stiffness tensor of the q-phase; ϕ_1 is the volume fraction of the nanoparticles, and $\mathbf{I}$ signifies the fourth-rank identity tensor [30,31,26,37].

At the nanoscale, the interface stress between a matrix and nano-inhomogeneities may have a significantly influence on the overall behavior of composites [4,24]. The interior-Eshelby tensor $\mathbf{S}$ for a nano-inhomogeneity with the interface effect is, therefore, considered in this study. Following the method proposed by Ju and Chen [10], Duan et al. [4], and Kim et al. [22], the volume-averaged Eshelby tensor for a nano-inhomogeneity $\mathbf{S}$ can be obtained using ensemble and volume-averaged procedures as follows:

$$\mathbf{S} = \Psi_1 \delta_{ij}\delta_{kl} + \Psi_2(\delta_{ik}\delta_{jl} + \delta_{il}\delta_{jk}) \tag{5}$$

with

$$\Psi_1 = -\frac{21}{5}\Lambda_1 - \Lambda_2 + \Lambda_3, \quad \Psi_2 = \frac{1}{2}\left(\frac{63}{5}\Lambda_1 + 3\Lambda_2 + 1\right) \tag{6}$$

where the parameters Λ_i (i = 1, 2, 3) are listed in the Appendix A (see also [4,22]. Combining Eq. (3) with Eq. (5), the effective elastic stiffness equation can be derived as (cf. [22])

$$\mathbf{C}_* = \widehat{C}_1 \delta_{ij}\delta_{kl} + \widehat{C}_2(\delta_{ik}\delta_{jl} + \delta_{il}\delta_{jk}) \tag{7}$$

where

$$\widehat{C}_1 = \kappa_0(1+\xi_2) - \frac{2}{3}\mu_0(1+\xi_1), \quad \widehat{C}_2 = \mu_0(1+\xi_1) \tag{8}$$

with

$$\xi_1 = \frac{-\phi_1(\mu_0 - \mu_1)}{\mu_0 + 2(\phi_1 - 1)(\mu_0 - \mu_1)\Psi_2} \tag{9}$$

$$\xi_2 = \frac{-\phi_1(\kappa_0 - \kappa_1)}{\kappa_1(1-\phi_1)(3\Psi_1 + 2\Psi_2) + \kappa_0\{1 + 3\Psi_1(\phi_1 - 1) + 2\Psi_2(\phi_1 - 1)\}} \tag{10}$$

where μ_q, κ_q, and v_q (q = 0, 1) are the shear modulus, bulk modulus and Poisson's ratio of the q-phase, respectively.

2.2. Effective elastoplastic behavior of nanopartice-reinforced composites

The effective elastoplastic behavior of nanoparticle-reinforced composites can be estimated by employing an ensemble-volume averaged homogenization procedure [38,40]. Upon deformation or loading continues to increase, the nanoparticle-reinforced composites may yield and become plastic [38]. Thus, the von Mises yield criterion is adopted in the present study to account for the effects of initial yielding and the plastic hardening law of the matrix [17]. Following Ju and Chen [11] and Ju et al. [12], the stress field in the matrix is considered to satisfy the effective yield function at any matrix point $\mathbf{x}$:

$$\overline{F} = \sqrt{\langle H \rangle_m(\mathbf{x})} - \mathbf{K}(\bar{\mathbf{e}}^{\mathbf{p}}) \leqslant \mathbf{0} \tag{11}$$

where $\bar{e}^p$ and $K(\bar{e}^p)$ are the equivalent plastic strain and the isotropic hardening function of the matrix, respectively. In addition, $\langle H \rangle_m(\mathbf{x})$ defines the ensemble average of $H(\mathbf{x}|\Omega)$ over all possible realizations for matrix point $\mathbf{x}$ [14]

$$\langle H \rangle_m(\mathbf{x}) \cong H^0 + \int_\Omega \left\{ H(\mathbf{x}|\Omega) - H^0 \right\} P(\Omega) d\Omega \tag{12}$$

in which $H^0 = \boldsymbol{\sigma}^0 : \mathbf{I}_d : \boldsymbol{\sigma}^0$ is the square of the far-field stress norm applied to the composites, $\mathbf{I}_d$ denotes the deviatoric part of the fourth-rank identity tensor $\mathbf{I}$, and $H(\mathbf{x}|\Omega) = \boldsymbol{\sigma}(\mathbf{x}|\Omega) : \mathbf{I}_d : \boldsymbol{\sigma}(\mathbf{x}|\Omega)$ denotes the square of the current stress norm at the local point $\mathbf{x}$ for a given nanoparticle configuration Ω [21]. $P(\Omega)$ signifies the probability density function to determine nanoparticle configuration Ω in the composites [19]. A more detailed description of the ensemble-averaged stress norm $\langle H \rangle_m(\mathbf{x})$ under the plane-strain condition can be found in Ju and Tseng [18], Ju and Lee [15], and Lee and Pyo [27].

The total stress at any point $\mathbf{x}$ in the matrix is the superposition of the far-field stress $\boldsymbol{\sigma}^0$ and the perturbed stress $\boldsymbol{\sigma}'$ due to existence of particles as $\boldsymbol{\sigma}(\mathbf{x}) = \boldsymbol{\sigma}^0 + \boldsymbol{\sigma}'$, with possible rephrasing as shown below [12]:

$$\boldsymbol{\sigma}(\mathbf{x}) = \boldsymbol{\sigma}^0 + \mathbf{C}_0 : \mathbf{G}(\mathbf{r}) : \boldsymbol{\epsilon}_1^{*0} \tag{13}$$

where $\boldsymbol{\epsilon}_1^{*0}$ is the eigenstrain tensor expressed explicitly for a spherical nanoparticle as $\boldsymbol{\epsilon}_1^{*0} = -\left\{(\mathbf{C}_1 - \mathbf{C}_0)^{-1} \cdot \mathbf{C}_0 + \mathbf{S}\right\}^{-1} : \boldsymbol{\epsilon}^0$ [39]. The exterior-Eshelby tensor for a spherical nano-inhomogeneity $\mathbf{G}(\mathbf{r})$ can be rephrased as follows (cf. [4]):

$$\begin{aligned}
\mathbf{G}(\mathbf{r}) = {} & \frac{15(7\gamma_2 - 6\gamma_1 h^2)}{2h^5} n_i n_j n_k n_l + \left(\frac{9\gamma_1 v_0}{h^3} - \frac{15\gamma_2}{2h^5}\right)(\delta_{ik} n_j n_l \\
& + \delta_{il} n_j n_k + \delta_{jk} n_i n_l + \delta_{jl} n_i n_k) + \left(\frac{9\gamma_1}{h^3} - \frac{15\gamma_2}{2h^5}\right)\delta_{ij} n_k n_l \\
& - \frac{3\left\{5\gamma_2 - 2(5\gamma_1 - \gamma_3)h^2 + 8\gamma_1 h^2 v_0\right\}}{2h^5}\delta_{kl} n_i n_j \\
& + \frac{3\gamma_2 - 2(5\gamma_1 - \gamma_3)h^2 + 8\gamma_1 h^2 v_0}{2h^5}\delta_{ij}\delta_{kl} \\
& + \frac{3(2\gamma_1 h^2 + \gamma_2 - 4\gamma_1 h^2 v_0)}{2h^5}(\delta_{ik}\delta_{jl} + \delta_{il}\delta_{jk})
\end{aligned} \tag{14}$$

with

$$\gamma_1 = -\frac{\Gamma\{5\Gamma(7+5v_1) - 4(3\kappa_s^r + \mu_s^r + 5)(10v_1 - 7)\}}{6\eta_{11}} \tag{15}$$

$$\gamma_2 = -\frac{\Gamma[3\Gamma(7+5v_1) - 4\{\kappa_s^r(1+v_0) + \mu_s^r(2v_0 - 1) + 3\}(10v_1 - 7)]}{3\eta_{11}} \tag{16}$$

$$\gamma_3 = \frac{\Gamma(1+v_1)}{3\{(\kappa_s^r + 2)(1-2v_1) + \Gamma(1+v_1)\}} \tag{17}$$

where $\mathbf{r} = r\mathbf{n}$ in which $\mathbf{n}$ is the unit vector, and the parameters η_{11} and η_{12} are given in the Appendix A (cf. [4,22]). In addition, $\Gamma = \mu_1/\mu_0, h = r/R$, and r is the distance from the center of the spherical inhomogeneities to any point $\mathbf{x}$. $\kappa_s^r = \kappa_s/(R\mu_0)$ and $\mu_s^r = \mu_s/(R\mu_0)$ are non-dimensional parameters, and $\kappa_r = 2(\mu_s + \lambda_s)$ in which λ_s and μ_s are the interface moduli are intrinsic physical properties of the interface [4,5].

After a series of lengthy derivations, the ensemble-averaged $\langle H\rangle_m$ can be determined as

$$\langle H\rangle_m(\mathbf{x}) = \boldsymbol{\sigma}^0 : \mathbf{T} : \boldsymbol{\sigma}^0 \tag{18}$$

where the components of the fourth-rank tensor $\mathbf{T}$ take the form

$$T_{ijkl} = T_1\delta_{ij}\delta_{kl} + T_2(\delta_{ik}\delta_{jl} + \delta_{il}\delta_{jk}) \tag{19}$$

with

$$T_1 = -\frac{1}{3} + \frac{\phi_1}{5}\left[24\mu_0^2\{45\gamma_3^2\chi_1^2 + 60\gamma_3^2\chi_1\chi_2 - 4\chi_2^2(\chi_3 - 5\gamma_3^2)\}\right] \tag{20}$$

$$T_2 = \frac{1}{2} + \frac{\phi_1}{5}(144\mu_0^2\chi_2^2\chi_3) \tag{21}$$

with

$$\chi_1 = \frac{\mu_0 - \mu_1}{6\mu_0\{\mu_0 + 2(\mu_1 - \mu_0)\Psi_2\}} + \frac{\kappa_0 - \kappa_1}{9\kappa_0\{\kappa_0(3\Psi_1 + 2\Psi_2 - 1) - 2\kappa_1(3\Psi_1 + 2\Psi_2)\}} \tag{22}$$

$$\chi_2 = \frac{\mu_0 - \mu_1}{4\mu_0\{\mu_0(2\Psi_2 - 1) - 2\mu_1\Psi_2\}} \tag{23}$$

$$\chi_3 = 40\gamma_1^2 - 36\gamma_1\gamma_2 + 15\gamma_2^2 + 4\gamma_1^2 v_0(7v_0 - 10) \tag{24}$$

The ensemble-averaged current stress norm $\boldsymbol{\sigma}^0$ can be expressed in terms of macroscopic stress $\bar{\boldsymbol{\sigma}}$ as follows [10]:

$$\boldsymbol{\sigma}^0 = \mathbf{P} : \bar{\boldsymbol{\sigma}} \tag{25}$$

where the fourth-rank tensor $\mathbf{P}$ can be expressed as

$$P_{ijkl} = P_1\delta_{ij}\delta_{kl} + P_2(\delta_{ik}\delta_{jl} + \delta_{il}\delta_{jk}) \tag{26}$$

with

$$P_1 = \frac{\phi_1\{2\beta_1\Psi_1 + \alpha_1(1 - 2\Psi_2)\}}{(\phi_1 + 2\beta_1 - 2\phi_1\Psi_2)(\phi_1 + 3\alpha_1 + 2\beta_1 - 3\phi_1\Psi_1 - 2\phi_1\Psi_2)} \tag{27}$$

$$P_2 = \frac{\beta_1}{\phi_1 + 2\beta_1 - 2\phi_1\Psi_2} \tag{28}$$

with

$$\alpha_1 = \frac{1}{3}\left(\frac{\kappa_0}{\kappa_1 - \kappa_0} - \frac{\mu_0}{\mu_1 - \mu_0} + 3\Psi_1\right), \quad \beta_1 = \frac{1}{2}\left(\frac{\mu_0}{\mu_1 - \mu_0} + 2\Psi_2\right) \tag{29}$$

Combination of Eqs. (18) and (25) leads to an alternative expression of the ensemble-averaged square of the current stress norm at the matrix as [16]

$$\langle H\rangle_m(\mathbf{x}) = \bar{\boldsymbol{\sigma}}^0 : \bar{\mathbf{T}} : \bar{\boldsymbol{\sigma}}^0 \tag{30}$$

where the components of the fourth-rank tensor $\bar{\mathbf{T}}$ are defined as

$$\bar{\mathbf{T}} \equiv \mathbf{P}^T \cdot \mathbf{T} \cdot \mathbf{P} \tag{31}$$

and can be shown to be

$$\bar{T}_{ijkl} = \bar{T}_1\delta_{ij}\delta_{kl} + \bar{T}_2(\delta_{ik}\delta_{jl} + \delta_{il}\delta_{jk}) \tag{32}$$

which can be shown to be

$$\bar{T}_1 = (3P_1 + 2P_2)^2 T_1 + 2P_1(3P_1 + 4P_2)T_2, \quad \bar{T}_2 = 4P_2^2 T_2 \tag{33}$$

The probabilistic ensemble-averaged current stress norm for any point $\mathbf{x}$ in the nanocomposites can be characterized as $\sqrt{\langle H\rangle_m(\mathbf{x})} = (1-\phi_1)\sqrt{\bar{\boldsymbol{\sigma}} : \bar{\mathbf{T}} : \bar{\boldsymbol{\sigma}}}$, and the effective yield function given in Eq. (11) becomes (cf. [12,14,20])

$$\bar{F} = (1-\phi_1)\sqrt{\bar{\boldsymbol{\sigma}} : \bar{\mathbf{T}} : \bar{\boldsymbol{\sigma}}} - K(\bar{e}^p) \tag{34}$$

where the isotropic hardening function $K(\bar{e}^p)$ is taken as [14]

$$K(\bar{e}^p) = \sqrt{\frac{2}{3}}[\sigma_y + h(\bar{e}^p)^q] \tag{35}$$

where σ_y signifies the initial yield stress, and h and q denote the linear and exponential isotropic hardening parameters, respectively. In addition, the effective ensemble-averaged plastic strain rate $\dot{\bar{\epsilon}}^p$ and the effective plastic strain rate $\dot{\bar{e}}^p$ required for obtaining the ensemble-averaged current stress norm were given in Eqs. (61) and (62) of Ju and Zhang [19].

3. Numerical simulations

A series of numerical simulations are carried out using i) various typical values for λ_s and μ_s and ii) MD simulation results [43,48] for λ_s and μ_s.

3.1. Numerical simulations using various typical interface moduli

A polyimide is used as the matrix with the Young's modulus $E_m = 4.2$ GPa, the Poisson's ratio $v_m = 0.40$, and the initial uniaxial yield stress $\sigma_y = 80$ MPa and the linear exponential isotropic hardening parameters $h = 280$ MPa and $q = 0.6$ [43]. In addition, the Young's modulus and the Poisson's ratio of the silica nanoparticles are adopted in accordance with [43] as $E_p = 88.7$ GPa and $v_p = 0.082$, respectively, where the subscripts m and p correspondingly represent the matrix and particle (Chen et al. [2]; [43]. Various typical interface moduli ($\lambda_s = 1.5$ N/m, $\mu_s = 1$ N/m; $\lambda_s = 3$ N/m, $\mu_s = 2$ N/m; $\lambda_s = 4.5$ N/m, $\mu_s = 3$ N/m) are considered in these simulations.

To investigate the interface effect of nanoparticles on the polymeric composites, we first conduct a parametric study of the interface moduli [43]. The volume fraction of the nanoparticles is assumed to be $\phi_1 = 0.1$. The effective Young's modulus and bulk modulus of the silica/polyimide nanocomposites with various interface moduli are exhibited in Fig. 1a and b. The solid line corresponds to the estimation without considering the interface effect and the dashed lines represent the predictions with the interface effect. It is shown from Fig. 1 that as the nanoparticle size continues to increase, the effective Young's and bulk moduli asymptotically converge, reaching a state without the interface effect [22]. A strong interface effect is noted when the nanoparticle size is small, whereas a weak influence of the interface moduli is observed beyond a particle size of 10 nm (cf. [4,5,22]).

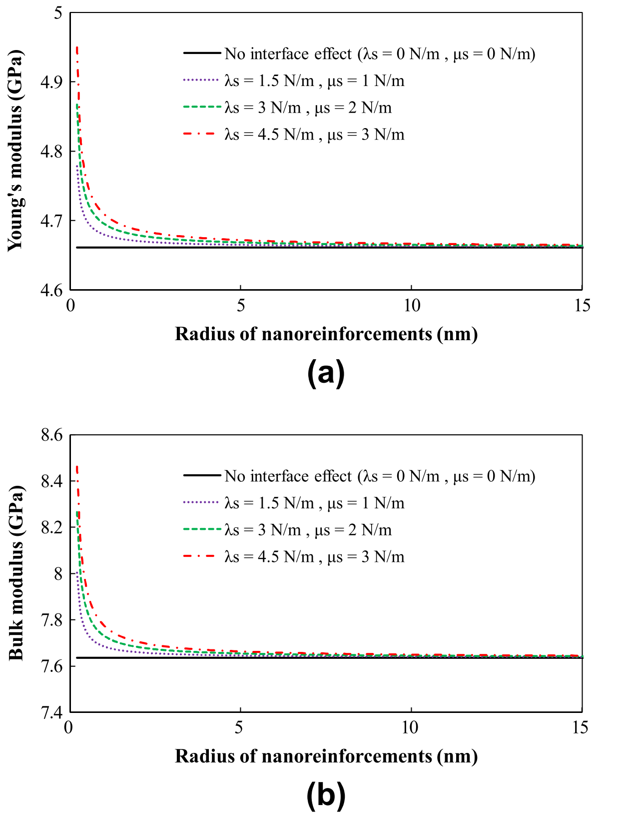

Fig. 1. The effective Young's modulus (a) and bulk modulus (b) of SiO_2/polyimide nanoparticle composites with respect to various interface moduli.

Figs. 2 and 3 show the effective stress–strain curves under uniaxial, biaxial and triaxial tension with various interface moduli. These figures exhibit tendencies similar to those of the numerical simulations in Fig. 1 in which the highest stress–strain responses are observed when the interface moduli $\lambda_s = 4.5$ N/m and $\mu_s = 3.0$ N/m, and the lowest stiffness as part of the stress–strain behavior is rendered at $\lambda_s = 0$ N/m and $\mu_s = 0$ N/m. The effect of the interface moduli is significant on the elastoplastic stress–strain responses under uniaxial loading conditions, whereas considerably less influence is observed in the case of biaxial and triaxial tension.

3.2. Numerical simulations using MD simulation results for interface moduli

In these simulations, the interface moduli of SiO_2 nanoparticle-reinforced polyimide composites are calculated based on the method proposed by Wang et al. [48] and MD simulation data from Odegard et al. [43]. When the interphase is thin and stiff, the interface moduli can be determined as [48]:

$$\lambda_s = \frac{2\mu_I \nu_I t}{(1-\nu_I)}, \quad \mu_s = \mu_I t \tag{36}$$

where μ_I, ν_I, and t denote the shear modulus, the Poisson's ratio, and the thickness of interface region [48]. Odegard et al. [43] computed the effective interface elastic properties of spherical silica/polyimide composites by means of MD simulations (see, Table 3 of [43]). The interface moduli of the SiO_2-reinforced polyimide can be, thus, estimated as: $\lambda_s = 1.44$ N/m and $\mu_s = 1.08$ N/m.

As shown in Fig. 4a, when the nanoparticle size increases, the overall behavior of the effective Young's modulus is generally reduced. It is clear from Fig. 4b that the effective bulk modulus also tends to decrease as the particle size increases. In addition, the effect of the volume fraction on the normalized Young's and bulk modulus with an increase in the radius of the nanoparticles is shown in Fig. 5. The interface effect gradually decreases as the particle size increases, and eventually diminishing when the particle size reaches 10 nm. Moreover, it is observed from Fig. 5a and b that the interface effect is more pronounced at a higher volume fraction of nanoparticles. It was demonstrated that the interface effect between the nanoparticles and the polymer matrix is fairly associated to a certain extent with the size and volume fraction of the nanoparticles.

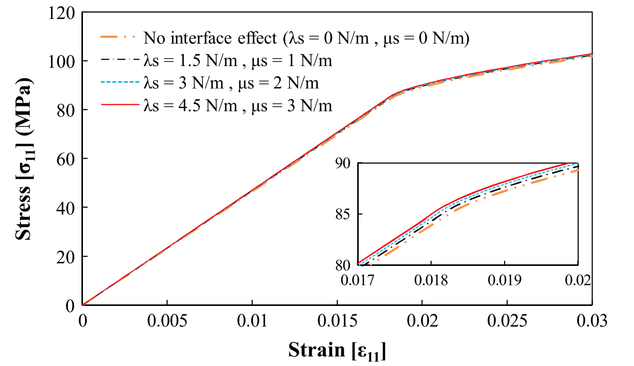

Fig. 2. The predicted stress–strain curves of nanoparticle-reinforced composites under uniaxial tensile loading with various interface moduli (λ_s, μ_s).

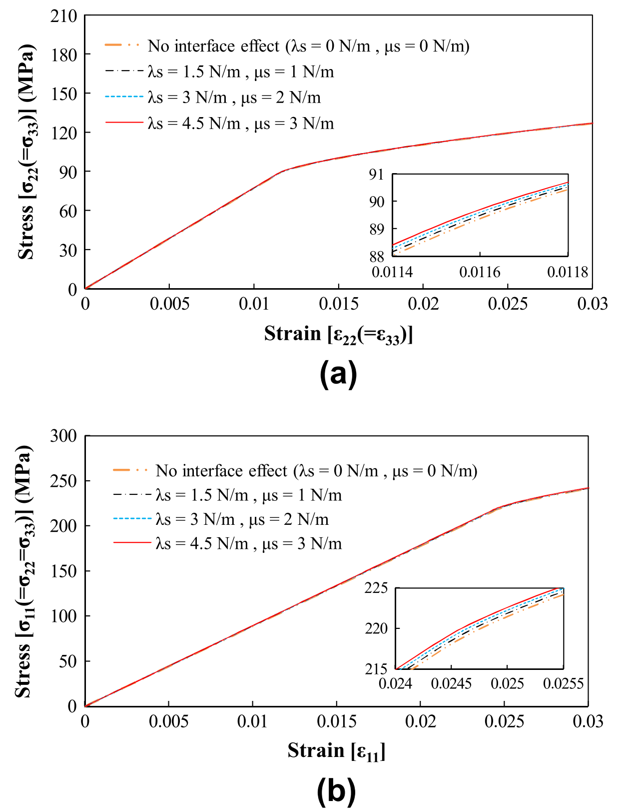

Fig. 3. The present predicted stress–strain responses under biaxial (a) and triaxial (b) tension with various values of interface moduli.

The effective stress–strain responses of nanoparticle-reinforced composites under uniaxial tension are illustrated in Fig. 6. Based on data reported by Odegard et al. [43], the radius of the nanoparticle is set to $R = 0.75$ nm. The present predictions in Fig. 6 exhibit a sudden change from the elastic to the plastic deformation shortly after

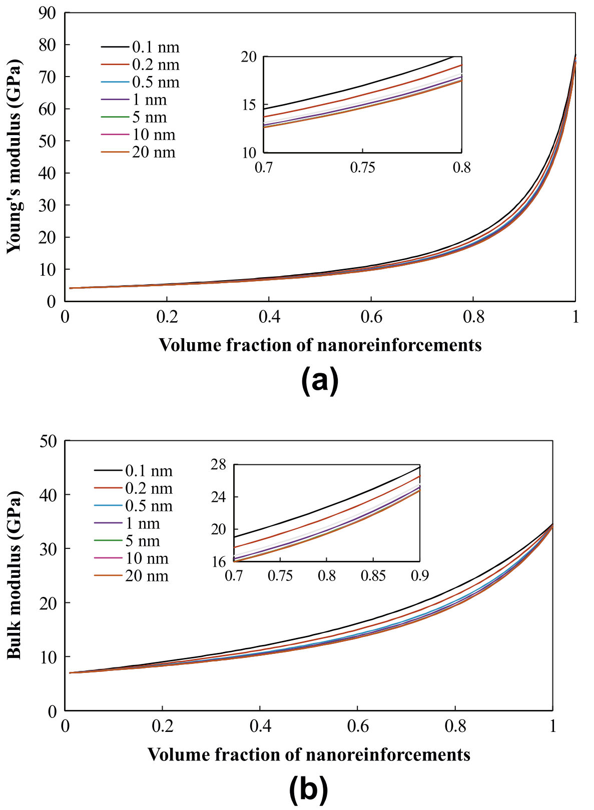

Fig. 4. The effective Young's modulus (a) and bulk modulus (b) of nanoparticle-reinforced composites considering various particle sizes versus the volume fraction.

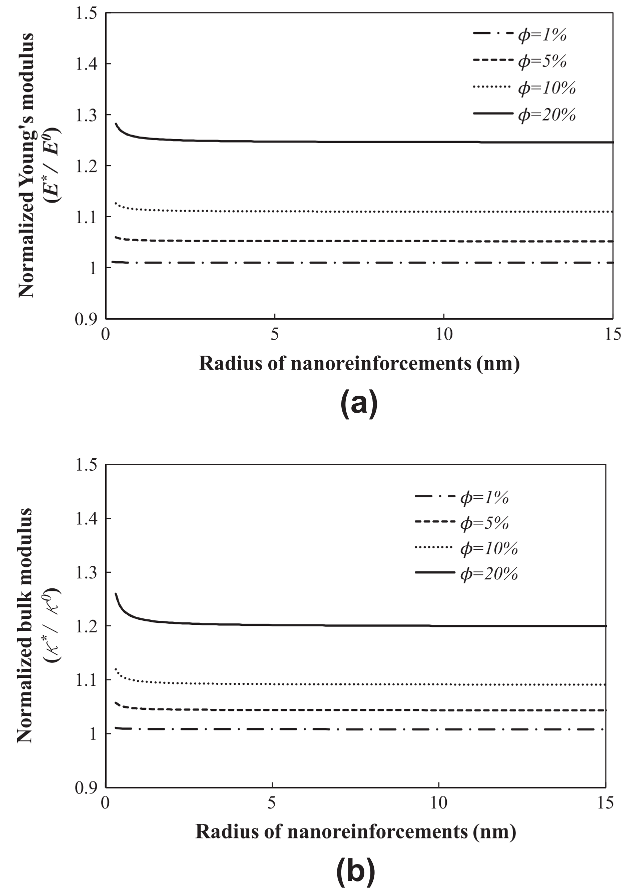

Fig. 5. Effects of the volume fraction of the nanoparticles (ϕ_1) on the normalized Young's modulus (a) and the bulk (b) modulus with an increase in the radius of the nanoreinforcements.

the yield point. It is apparent in the figure that the initial yield strength, plastic hardening modulus and Young's modulus increase as the volume fraction of the nanoparticles increases. This result shows the strengthening effect of the inclusion on the overall behavior of the nanoparticle-reinforced composites. The proposed model is further utilized to predict the effective stress–strain curves of the composites under various axisymmetric loading conditions. Fig. 7a and b exhibits the predicted mechanical responses under biaxial tension ($[\sigma_{22}(=\sigma_{33})]/\sigma_y$ versus $\epsilon_{22}(=\epsilon_{33})$) and triaxial tension ($[\sigma_{11}(=\sigma_{22}/=\sigma_{33}]/\sigma_y$ versus ϵ_{11}), respectively. As displayed in Figs. 6 and 7, the overall responses show higher stiffness in the elastic and plastic range as the volume fraction of the nanoparticle increases. It is also observed from the figures that a higher volume fraction of the nanoparticles leads to a higher yield strength of the composites.

To investigate the effect of the nanoparticle size on the overall elastoplastic behavior, the composites with varying radii of the nanoparticles R subject to uniaxial tensile loading are considered. As shown in Fig. 8, as the radius of nanoparticles increases from 0.1 nm to 10 nm, the effective stress–strain responses exhibit lower stiffness of the composites. This mainly arises due to the reason that the interface effect of the nanoparticles is pronounced as the radius of these particles decreases. Fig. 9a displays the results of numerical simulations under the biaxial tensile loading in the case of σ_{22} versus ϵ_{22}. It is clear from this figure that the effect of the particle size in the nanocomposites is quite influential compared to the case of uniaxial tensile loading. As rendered in Fig. 8, when the size of the nanoparticles increases (0.1, 0.2, 0.5, 1, and 10 nm), the effective stress–strain curves exhibit lower stiffness in both the elastic and the plastic ranges. The effect of the nanoparticle radius R on the elastoplastic behavior of nanocomposites under triaxial tensile loading for σ_{11} versus ϵ_{11} is also illustrated in Fig. 9b. In

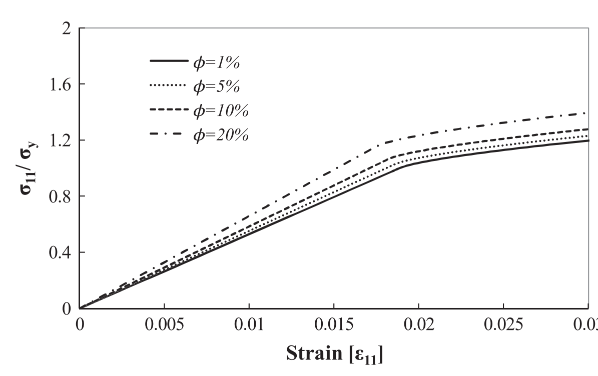

Fig. 6. Effects of the volume fractions of the nanoparticles on the normalized uniaxial elastoplastic behavior of nanocomposites.

Figs. 8 and 9, the nanocomposites show the highest stiffness and yield strength when triaxial tensile loading is applied; relatively higher elastoplastic behavior can be observed for the nanocomposites with smaller nanoparticles. It can be concluded from the aforementioned simulations that the effective mechanical properties of the nanocomposites are significantly affected by the interface effect, size, and volume fraction of nanoparticles. In particular, it is noted that as the volume fraction of nanoparticles continues to increase, the interface effect tends to increase, eventually increasing the overall stiffness of the nanocomposites.

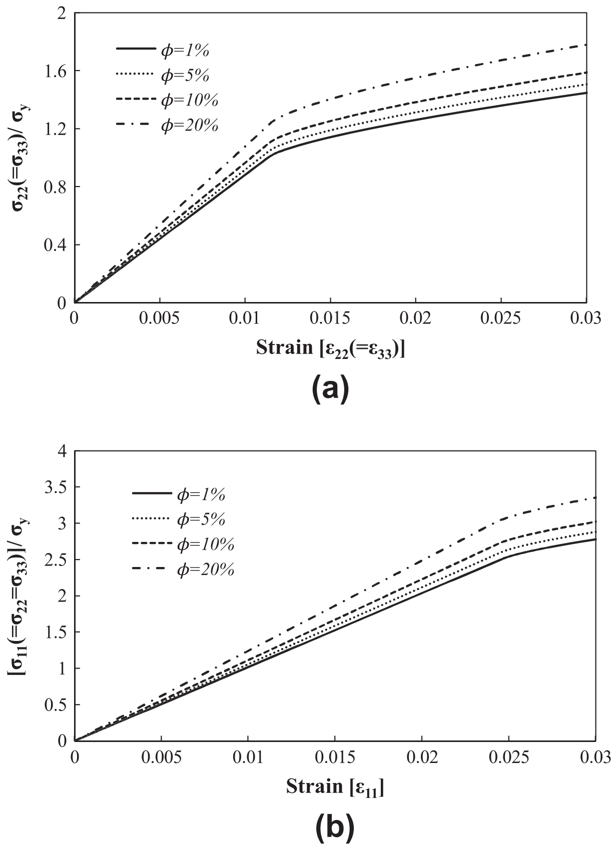

Fig. 7. The overall stress–strain responses of nanoparticle-reinforced composites during a biaxial (a) and triaxial tension (b) simulation.

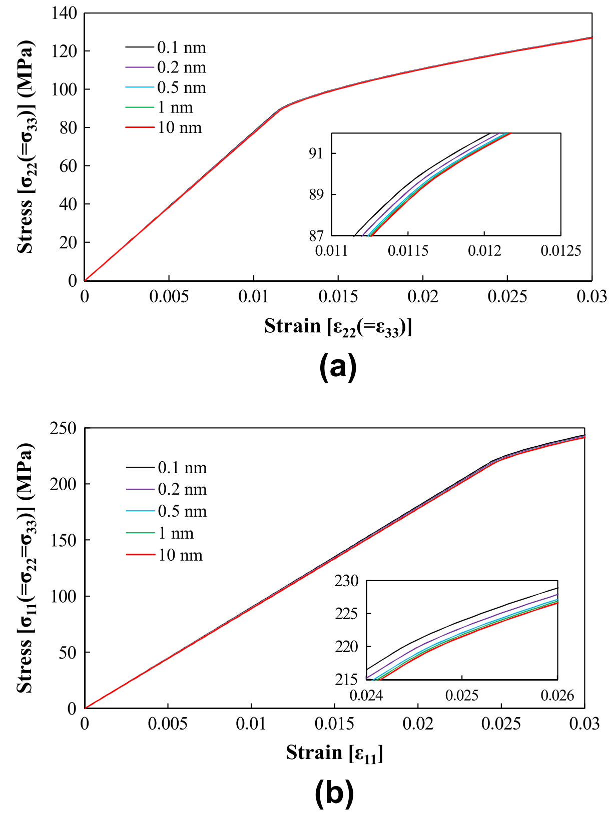

Fig. 9. The biaxial (a) and triaxial tension (b) stress–strain relationships of nanoparticlereinforced composites with a volume fraction of 10% with various sizes.

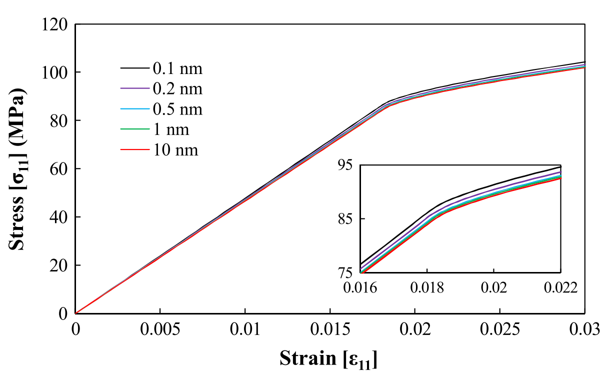

Fig. 8. Overall stress–strain relationships of nano-sized SiO_2/polyimide composites ($\phi_1 = 10\%$) for various values of R under uniaxial loading.

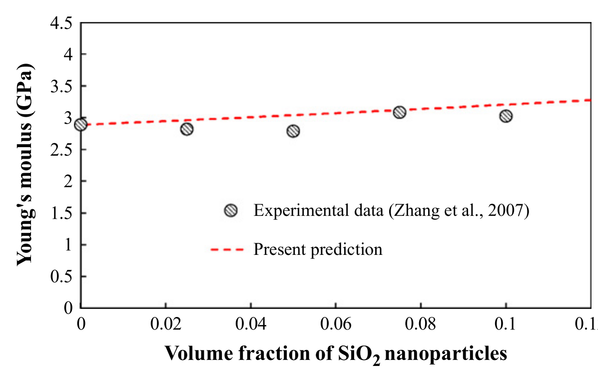

Fig. 10. Comparisons of the Young's modulus with the experimental data and the present prediction for silica inclusion/polyimide composites.

4. Experimental comparisons

To illustrate the predictive capability of the proposed model, comparisons are made between the present predictions and experimental data [53,42]. The material properties of the matrix and nanoparticles are identical to those in [53] as $E_m = 2.89$ GPa, $\nu_m = 0.30$ for the polyimide matrix, and $E_p = 73$ GPa, $\nu_p = 0.17$, $R = 40$ nm for the silica inclusion. The interface moduli are assumed as $\lambda_s = 1.44$ N/m and $\mu_s = 1.08$ N/m. The effective Young's modulus of composites is often referred to as an important indication of the mechanical behavior [47]. A prediction of the effective Young's modulus of nanocomposites with different volume fractions is, therefore, conducted here to demonstrate the capability of the proposed formulation. Fig. 10 shows the comparison between the predictions and the experimental results [53]. The result shows that the present predictions are in good agreement with the experimental data of the effective Young's moduli [53].

Fig. 11 shows comparisons between the present predictions and the experimental data quoted by Naito et al. [42]. The uniaxial stress–strain curves of the experiments were recorded at 23 °C for nano-SiO_2/polyimide composites. The reported elastic moduli and Poisson's ratio of the matrix and the nanoparticles are $E_m = 3.77$ GPa and $\nu_m = 0.342$ for the polyimide matrix and $E_p = 72$ GPa, $\nu_p = 0.17$, and $R = 40$ nm for the nano-SiO_2 [42]. The volume fractions of nanoparticles are respectively 1% and 10%, and the following plastic parameters are employed: $\sigma_y = 80$ MPa, $h = 280$ MPa and $q = 0.6$. Moreover, the interface moduli are obtained using Eq. (36) as: $\lambda_s = 1.44$ N/m and $\lambda_s = 1.08$ N/m. Note

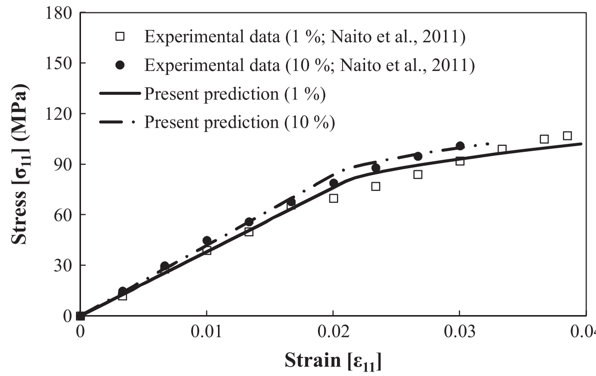

Fig. 11. Comparisons between the experimental data [42] and the present predictions of the nanocomposites (1% and 10%) under uniaxial tensile loading.

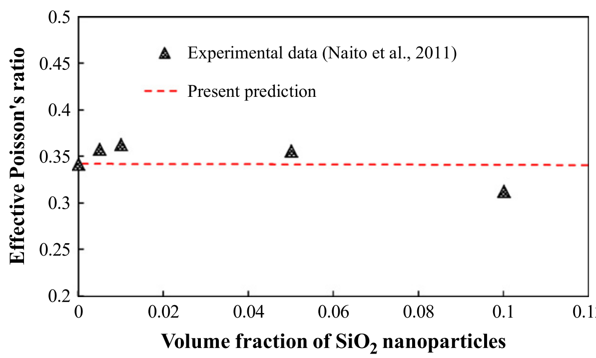

Fig. 12. Comparisons of effective Poisson's ratio with the experimental data [42] and the present predictions for nanosized SiO_2/polyimide composites.

that the plastic parameters and interface moduli are fitted at $\phi_1 = 1\%$ after which the estimated values are applied to the 10% case.

Naito et al. [42] also investigated the effective Poisson's ratio of nano-sized silica particle-reinforced composites. The material properties and interface moduli used here are identical to those used earlier. As depicted in Fig. 12, it is observed that the present predictions match well with the experimental data for the nanoparticle-reinforced composites. Overall, it is shown from Figs. 10–12 that the present predictions match well with the experimental data, showing the predictive capability of the proposed micromechanical elastoplastic model considering the interface effect.

5. Conclusions

A micromechanical model is proposed to predict the overall elastoplastic behavior of nanoparticle-reinforced polymeric composites, and to investigate the effect of nano-inclusion in the composites. The effects of interface and size of the nanoparticle are considered by means of the Eshelby tensor for a spherical nano-inhomogeneity []. With an ensemble volume-averaged homogenization procedure [23,35,28], the effective yield criterion and the elastoplastic behavior of nanocomposites are predicted. A series of numerical simulations are performed to investigate the influence of the radius and the interface moduli of the nanoparticles on the overall behavior of composites. The current micromechanical model is also applied to various loading conditions of uniaxial, biaxial and triaxial tension to predict the corresponding effective stress–strain responses. The findings from the numerical simulations can be summarized as follows:

(1) The interface effect of the nanoparticles decreases as the particle size continues to increase, and ultimately reaching a state without an interface effect.
(2) The interface effect is associated with the volume fraction of the nanoparticles, and is more pronounced at a higher volume fraction of nanoparticles.
(3) Stiffer stress–strain responses are displayed as the radius of the nanoparticles decreases and as the volume fraction of the nanoparticles increases.

The present predictions under a uniaxial tensile loading condition are compared with the experimental data reported by Zhang et al. [53] and Naito et al. [42]. The predictions based on the proposed model are generally in good agreement with the experimental data. The proposed methodology is expected to offer a wide range of predictive capacity of nanoparticle-reinforced composites and is likely to be suitable for more precise predictions of nanocomposites as well. The present micromechanical elastoplastic model with the interface effect will be extended to consider various problems induced by nano-inhomogeneities; however, additional numerical tests and experimental comparisons are necessary to assess the parameters used in the proposed model.

Acknowledgements

This research was supported by grants from the Construction Technology Innovation Program (11CCTI-B050520-04-000000) and the U-City Master and Doctor Course Grant Program (07High Tech A01) funded by the Ministry of Land, Transportation and Maritime Affairs of the Korean government.

Appendix A. The elastic parameters Λ_i (i = 1, 2, 3) in Eq. (6) (cf. [4,22])

$$\Lambda_1 = \frac{2\Gamma(4-5\nu_0)(\kappa_s^r+2\mu_s^r)}{3\eta_{11}}, \quad \Lambda_2 = \frac{\eta_{12}}{3\eta_{11}} \tag{37}$$

$$\Lambda_3 = -\frac{(1-2\nu_1)(2+\kappa_s^r)}{3\left[\Gamma(1+\nu_1)+(1-2\nu_1)(2+\kappa_s^r)\right]} \tag{38}$$

with

$$\begin{aligned}\eta_{11} = &-2\Gamma^2(7+5\nu_1)(4-5\nu_0) - 7\Gamma(39+20\kappa_s^r+16\mu_s^r)\\ &+35\nu_0\Gamma(9+5\kappa_s^r+4\mu_s^r)+\nu_1\Gamma(285+188\kappa_s^r+16\mu_s^r)\\ &-5\nu_0\nu_1\Gamma(75+47\kappa_s^r+4\mu_s^r)-4(7-10\nu_1)(7+11\mu_s^r)\\ &+4(7-10\nu_1)\left[-\kappa_s^r(5+4\mu_s^r)+\nu_0(5+4\kappa_s^r+13\mu_s^r+5\kappa_s^r\mu_s^r)\right]\end{aligned} \tag{39}$$

$$\begin{aligned}\eta_{12} = &\,4(7-10\nu_1)\left[7+11\mu_s^r+\kappa_s^r(5+4\mu_s^r)\right.\\ &\left.-\nu_0(5+4\kappa_s^r+13\mu_s^r+5\kappa_s^r\mu_s^r)\right]+7\Gamma(7-5\nu_0+5\nu_0\kappa_s^r-4\kappa_s^r)\\ &+\nu_1\Gamma(35+4\kappa_s^r+48\mu_s^r)-5\nu_0\nu_1\Gamma(5+\kappa_s^r+12\mu_s^r)\end{aligned} \tag{40}$$

where ν_0 and ν_1 are the Poisson's ratio of matrix and nanoparticles.

References

[1] Anumandla V, Gibson RF. A comprehensive closed form micromechanics model for estimating the elastic modulus of nanotube-reinforced composites. Compos A: Appl Sci Manuf 2006;37:2178–85.
[2] Chen Q, Chasiotis I, Chen C, Roy A. Nanoscale and effective mechanical behavior and fracture of silica nanocomposites. Compos Sci Technol 2008;68:3137–44.
[3] Colombini D, Hassander H, Karlsson OJ, Maurer FHJ. Influence of the particle size and particle size ratio on the morphology and viscoelastic properties of bimodal hard/soft latex blends. Macromolecules 2004;37:6865–73.

[4] Duan HL, Wang HT, Huang ZP, Karihaloo BL. Eshelby formalism for nano-inhomogeneities. P Roy Soc A – Math Phys 2005;461:3335–53.
[5] Duan HL, Wang J, Huang ZP, Luo ZY. Stress concentration tensors of inhomogeneities with interface effects. Mech Mater 2005;37:723–36.
[6] Eshelby JD. The determination of the elastic field of an ellipsoidal inclusion, and related problems. P Roy Soc A – Math Phys 1957;241:376–96.
[7] Fu SY, Feng XQ, Lauke B, Mai YW. Effects of particle size, particle/matrix interface adhesion and particle loading on mechanical properties of particulate–polymer composites. Compos B: Eng 2008;39:933–61.
[8] Hong Z, Chen J, Feng J, Du Y, Yu J, Zhang L, et al. Computer simulation of mechanical properties of nano-scale Cu/FeS composite. J Mater Sci 2010;26:337–43.
[9] Huang ZM, Zhang YZ, Kotaki M, Ramakrishna S. A review on polymer nanofibers by electrospinning and their applications in nanocomposites. Compos Sci Technol 2003;63:2223–53.
[10] Ju JW, Chen TM. Micromechanics and effective elastoplastic behavior of two-phase metal matrix composites. J Eng Mater – Trans ASME 1994;116:310–8.
[11] Ju JW, Chen TM. Micromechanics and effective moduli of elastic composites containing randomly dispersed ellipsoidal inhomogeneities. Acta Mech 1994;103:103–21.
[12] Ju JW, Ko YF, Ruan HN. Effective elastoplastic damage mechanics for fiber-reinforced composites with evolutionary complete fiber debonding. Int J Damage Mech 2006;15:237–65.
[13] Ju JW, Ko YF, Ruan HN. Effective elastoplastic damage mechanics for fiber reinforced composites with evolutionary partial fiber debonding. Int J Damage Mech 2008;17:265–493.
[14] Ju JW, Ko YF. Micromechanical elastoplastic damage modeling of progressive interfacial arc debonding for fiber reinforced composites. Int J Damage Mech 2008;17:307–54.
[15] Ju JW, Lee HK. A micromechanical damage model for effective elastoplastic behavior of ductile matrix composites considering evolutionary complete particle debonding. Comput Method Appl M 2000;183:201–22.
[16] Ju JW, Lee HK. A micromechanical damage model for effective elastoplastic behavior of partially debonded ductile matrix composites. Int J Solids Struct 2001;38:6307–32.
[17] Ju JW, Tseng KH. Effective elastoplastic behavior of two-phase ductile matrix composites: a micromechanical framework. Int J Solids Struct 1996;33:4267–91.
[18] Ju JW, Tseng KH. Effective elastoplastic algorithms for ductile matrix composites. J Eng Mech 1997;123:260–6.
[19] Ju JW, Zhang XD. Effective elastoplastic behavior of ductile matrix composites containing randomly located aligned circular fibers. Int J Solids Struct 2001;38:4045–69.
[20] Pyo SH, Lee HK. An elastoplastic damage model for metal matrix composites considering progressive imperfect interface under transverse loading. Int J Plasticity 2010;26:25–41.
[21] Kim BR, Lee HK. Elastoplastic modeling of circular fiber-reinforced ductile matrix composites considering a finite RVE. Int J Solids Struct 2010;47:827–36.
[22] Kim BR, Pyo SH, Lemaire G, Lee HK. Multiscale approach to predict the effective elastic behavior of nanoparticle-reinforced polymer composites. Interact Multisc Mech 2011;4:173–85.
[23] Lee HK. A computational approach to the investigation of impact damage evolution in discontinuously reinforced fiber composites. Comput Mech 2001;27:504–12.
[24] Lee HK, Ju JW. 3-D micromechanics and effective moduli for brittle composites with randomly located interacting microcracks and inclusions. Int J Damage Mech 2008;17:377–417.
[25] Lee HK, Kim BR. Numerical characterization of compressive response and damage evolution in laminated plates containing a cutout. Compos Sci Technol 2007;67:2221–30.
[26] Lee HK, Pyo SH. Micromechanics-based elastic damage modeling of particulate composites with weakened interfaces. Int J Solids Struct 2007;44:459–74.
[27] Lee HK, Pyo SH. An elastoplastic multi-level damage model for ductile matrix composites considering evolutionary weakened interface. Int J Solids Struct 2008;45:1614–31.
[28] Lee HK, Pyo SH. Multi-level modeling of effective elastic behavior and progressive weakened interface in particulate composites. Compos Sci Technol 2008;68:387–97.
[29] Lee HK, Shin DK. A computational investigation of crack evolution and interactions of microcracks and particles in particle-reinforced brittle composites. Compos Struct 2004;64:419–31.
[30] Lee HK, Simunovic S. Modeling of progressive damage in aligned and randomly oriented discontinuous fiber polymer matrix composites. Compos B: Eng 2000;31:77–86.
[31] Lee HK, Simunovic S. A damage constitutive model of progressive debonding in aligned discontinuous fiber composites. Compos B: Eng 2001;38:875–95.
[32] Lee HK, Simunovic S. A damage mechanics model of crack-weakened, chopped fiber composites under impact loading. Compos B: Eng 2002;33:25–34.
[33] Lee HK, Simunovic S. Prediction of crack evolution and effective elastic behavior of damage-tolerant brittle composites. Comput Method Appl M 2006;196:118–33.
[34] Lee HK, Simunovic S, Shin DK. A computational approach for prediction of the damage evolution and crushing behavior of chopped random fiber composites. Compos Mater Sci 2004;29:459–74.
[35] Lee HK, Liang Z. Computational modeling of the response and damage behavior of fiber-reinforced cellular concrete. Comput Struct 2004;82:581–92.
[36] Li G, Helms JE, Pang SS, Schulz K. Analytical modeling of tensile strength of particulate filled composites. Polym Compos 2001;22:593–603.
[37] Liang Z, Lee HK, Suaris W. Micromechanics-based constitutive modeling for unidirectional laminated composites. Int J Solids Struct 2006;43:5674–89.
[38] Liu HT, Sun LZ, Ju JW. Multi-scale modeling of elastoplastic deformation and strengthening mechanisms in aluminum-based amorphous nanocomposites. Acta Mater 2005;53:2693–701.
[39] Liu HT, Sun LZ, Ju JW. Elastoplastic modeling of progressive interfacial debonding for particle-reinforced metal–matrix composites. Acta Mech 2006;118:1–17.
[40] Liu HT, Sun LZ, Ju JW. A micromechanics-based elastoplastic model for amorphous composites with nanoparticle interactions. J Appl Mech – Trans ASME 2008;75:1–10.
[41] Luo YC, Liu R, Li DY. Investigation of the mechanism for the improvement in wear resistance of nano-TiN/TiC/TiNi composite: a study combining experiment and FEM analysis. Mater Sci Eng A: Struct 2002;329:768–73.
[42] Naito K, Yang JM, Kagawa Y. The effect of nanoparticle inclusion on the tensile and mode I fracture properties of polyimides. Mater Sci Eng A 2011;530:357–66.
[43] Odegard GM, Clancy TC, Gates TS. Modeling of the mechanical properties of nanoparticle/polymer composites. Polymer 2005;46:553–62.
[44] Pacheco-Torgal F, Jalali S. Nanotechnology: advantages and drawbacks in the field of construction and building materials. Constr Build Mater 2011;25:582–90.
[45] Pyo SH, Lee HK. Micromechanical analysis of aligned and randomly oriented whisker-/short fiber-reinforced composites. CMES – Compos Model Eng Sci 2009;40:271–305.
[46] Sun L, Gibson RF, Gordaninejad F. Multiscale analysis of stiffness and fracture of nanoparticle-reinforced composites using micromechanics and global–local finite element models. Eng Fract Mech 2011;78:2645–62.
[47] Sun LZ, Liu HT, Ju JW. Effect of particle cracking on elastoplastic behaviour of metal matrix composites. Int J Numer Meth Eng 2003;56:2183–98.
[48] Wang J, Duan HL, Zhang Z, Huang ZP. An anti-interpenetration model and connections between interphase andinterface models in particle-reinforced composites. Int J Mech Sci 2005;47:701–18.
[49] Yao XF, Yeh HY, Zhou D, Zhang YH. The structural characterization and properties of SiO_2-epoxy nanocomposites. J Compos Mater 2006;40:371–81.
[50] Yang BJ, Kim BR, Lee HK. Predictions of viscoelastic strain rate dependent behavior of fiber-reinforced polymeric composites. Compos Struct 2012;94:1420–9.
[51] Yang BJ, Kim BR, Lee HK. Micromechanics-based viscoelastic damage model for particle-reinforced polymeric composites. Acta Mech 2012;223:1307–21.
[52] Yang S, Cho M. A scale-bridging method for nanoparticulate polymer nanocomposites and their nondilute concentration effect. Appl Phys Lett 2009;94:223104.
[53] Zhang Q, Naito K, Kagaw Y. Synthesis and mechanical properties of advanced polyimide/silicon dioxide nanocomposites. Mater Sci Forum 2007;561–565:709–12.